AAS 25-427

COMPUTATION OF INVARIANT TORI IN THE HILL RESTRICTED FOUR-BODY PROBLEM VIA COLLOCATION

Guido Grossi*, Francesco Topputo †

The Hill Restricted Four-Body Problem offers a promising framework for analyzing spacecraft dynamics in the Sun–Earth–Moon system. This study explores the computation of families of quasi-periodic orbits, or 2-dimensional invariant tori, that emerge from isolated periodic orbits, opening up new possibilities for advanced trajectory design. The outlined method combines the Fourier discretization of an invariant curve of a stroboscopic map with a Gauss–Legendre collocation scheme. Stability analysis is performed as a by-product of the implementation. Compared to the shooting-based variants of the algorithm, the collocation approach demonstrated superior efficiency while providing a continuous representation of the tori.

INTRODUCTION

In recent decades, there has been a renewed surge of interest in leveraging the Earth–Moon system for space missions to the Moon and beyond. The intricate dynamics in the cislunar and circumlunar regions pose challenges for efficient preliminary path planning from Earth, as well as for operations around the Moon. However, establishing a framework that leverages dynamical structures and harnesses the Sun's gravitational influence can facilitate trajectory design in this regime. To this aim, various astrodynamical models have been proposed, from the classical Circular Restricted Three-Body Problem (CRTBP) to more advanced ephemeris models of the complete solar system.[1,2]

The CR3BP is a widely used model for describing the cislunar environment.[3] However, it does not account for the Sun's influence on spacecraft (direct effect) and on the Earth and Moon (indirect effect).[4] Therefore, to effectively utilize natural dynamical structures for trajectory design, a four-body problem should be considered. Notably, in such models, invariant solutions can still exist.[5]

The simplest four-body problem for the Sun–Earth–Moon system is the Bicircular Restricted Four-Body Problem (BR4BP).[6] The dynamical structures of this problem have been extensively studied.[7–10] The BR4BP accounts for the Sun's direct effect while neglecting its indirect influence, resulting in a simple yet incoherent model. To address these issues, the Quasi-Bicircular Restricted Four-Body Problem (QBR4BP) was introduced and studied in detail.[11–13] In this model, the motion of the three primary bodies is determined using a solution to the general planar three-body problem. The result is a coherent model, particularly suited for studying the motion in the Sun–Earth–Moon system. However, preserving coherence in this manner comes at the cost of significant model complexity which makes the analysis of its dynamics computationally expensive.[14,15]

*Ph.D. Student, Department of Aerospace Science and Technology, Politecnico di Milano, via La Masa, 34, Milan, 20156, Italy; guido.grossi@polimi.it

†Full Professor, Department of Aerospace Science and Technology, Politecnico di Milano, via La Masa, 34, Milan, 20156, Italy; francesco.topputo@polimi.it

The Hill Restricted Four-Body Problem (HR4BP), first introduced in Reference 16, provides an alternative framework for modeling the Sun–Earth–Moon system. In this paradigm, a periodic solution from Hill Three-Body Problem is used for the orbits of the primary bodies.[17–20] By applying Hill's approximation, the model maintains coherence while preserving a level of simplicity.[21] Moreover, the HR4BP can be seen as a periodic perturbation of the CR3BP. Consequently, invariant objects from the latter become objects one dimension higher in the HR4BP. Equilibrium points turn into periodic orbits, and (non-resonant) periodic orbits become quasi-periodic orbits.[5] Some recent works have focused on describing the phase-space structure around the dynamical substitutes of the CR3BP equilibrium points, and computing families of periodic and quasi-periodic orbits.[4,14,16,22–26] Despite being less studied compared to other models, the HR4BP offers a unique balance of advantages over the BR4BP and QBR4BP, making it a promising alternative.

Quasi-periodic motion is one of the fundamental dynamical structures found in periodic Hamiltonian systems like the HR4BP. In particular, quasi-periodic orbits that originate from periodic orbits are of significant interest to the astrodynamics community. Indeed, they can further extend the design space by providing mission designers with new tools.[27–31] These trajectories lie on quasi-periodic invariant tori of dimension two or higher. Several strategies, both analytical and semi-analytical, have been developed throughout the last decade to compute invariant tori in astrodynamics. A comprehensive survey on the numerical methods can be found in Reference 32.

Among these methods, Gómez and Mondelo introduced a numerical technique for calculating the Fourier coefficients of an invariant curve based on stroboscopic mapping.[33] This method was later refined by Olikara and Scheeres to operate directly on orbital states.[24] The resulting procedure, commonly referred to as GMOS, has become recognized as the most efficient numerical method for studying families of quasi-periodic orbits.[32]

One of the most widely used versions of GMOS solves a two-point boundary value problem for invariant curves through multiple shooting. However, a collocation-based approach was first outlined in Reference 28. Unlike the shooting technique, the collocation version approximates quasi-periodic trajectories using piecewise continuous polynomials instead of relying on numerical integration. As noted in Reference 27, collocation allows for the computation of quasi-periodic invariant tori even with poor initial guesses, offering significant numerical stability and a large basin of attraction. Moreover, the methodology proposed in Reference 28 introduced an unfolding parameter that significantly improves the efficiency of solving the system of algebraic equations derived from Newton's method. Despite involving a larger number of unknowns, the collocation-based GMOS has proven to be considerably faster and more efficient than its shooting-based counterparts (see Chapter 3.5 of Reference 27 for a quantitative comparison). Additionally, this approach directly yields a continuous representation of the entire torus, eliminating the need for the post-processing steps required by shooting-based methods.

This paper focuses on computing families of two-dimensional invariant tori and their stability within the HR4BP using an efficient collocation-based method. The primary goal is to describe the method and adapt it to the HR4BP, demonstrating it as an effective alternative to the shooting version used in previous studies.[4,14,22,23] Another aim is to investigate quasi-periodic orbits and deepen the understanding of the natural motion in the cislunar environment. Ultimately, identifying higher-dimensional invariant manifolds (which lie within larger parameter families in the phase space) not only enriches academic research but also opens new avenues for space mission, providing innovative tools for trajectory design.

BACKGROUND

Hereafter, we provide an overview of the Hill Restricted Four-Body Problem and discuss some periodic orbits that serve as cornerstones for understanding the system dynamical behavior. Subsequently, we introduce the theory of invariant tori.

Hill Restricted Four-Body Problem

The HR4BP describes the motion of a particle P_3 under the gravitational influence of three massive bodies $P_{0,1,2}$. For a comprehensive derivation of the model see Reference 16. The HR4BP is based on the following key assumptions: (I) the mass of the largest primary, P_0, is significantly greater than the masses of the other two primaries, P_1 and P_2; (II) the mass of the particle, P_3, is negligible; (III) the distances between the three smaller bodies are much shorter than their distance from the largest primary. In the Sun–Earth–Moon system, P_0 corresponds to the Sun, P_1 to the Earth, and P_2 to the Moon. Under these assumptions, both the Sun and the Earth–Moon barycenter (EMB) follow Keplerian orbits, and the relative motion between the Earth and the Moon can be described by a solution to the Hill Three-Body Problem.[21] In the HR4BP, the orbit of the Sun around the EMB is assumed to be circular, while the relative motion of the Earth and the Moon is modeled using a member of a planar family of periodic orbits known as Hill's variation orbits.[17–20] These orbits, initially introduced by Hill to approximate the Earth–Moon motion, are characterized by a single parameter, m, which represents the synodic period of the Earth–Moon orbit in years. For the Sun–Earth–Moon system, the value of this parameter is $m = 0.0808$.

The motion of P_3 is analyzed in a reference frame $(\hat{\mathbf{e}}_x, \hat{\mathbf{e}}_y, \hat{\mathbf{e}}_z)$ centered at the EMB, which rotates around $\hat{\mathbf{e}}_z$ at a constant absolute rate $\Omega = 1 + 1/m$, where 1 is the normalized rotation rate of the EMB around the Sun, and $1/m$ is the average rotation rate of the Earth–Moon orbit. Its definition is similar to that of the synodic frame in the Earth–Moon CR3BP. However, in the HR4BP, because the Earth and Moon do not follow a circular orbit, the bodies are not stationary in the frame but instead oscillate around their average positions. The axis $\hat{\mathbf{e}}_x$ points from the EMB to the average position of the Moon, $\hat{\mathbf{e}}_z$ aligns with the direction of the angular momentum of the two primaries, and $\hat{\mathbf{e}}_y$ completes the right-handed coordinate system. Length is normalized using the average Earth–Moon distance (384,400 km) and time such that one synodic month (29.53 days) corresponds to 2π time units. A sketch of the HR4BP is shown in Figure 1.

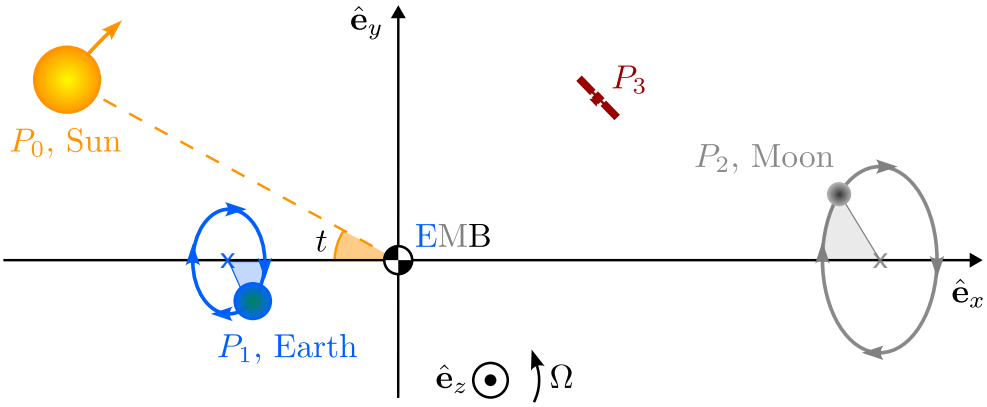

Figure 1. Sketch of the Hill Restricted Four-body Problem in the rotating Earth–Moon frame (drawing not to scale; in particular, the orbits of the Moon and Earth are exaggerated)

The Hill variation orbit that describes the relative motion of the Earth and Moon is represented as a Fourier series[23]

$$\mathbf{r}_{v.o.}(t) = \begin{pmatrix} 1 + \sum_{n=1}^{\infty} \left(\frac{a_n}{a_0}(m) + \frac{a_{-n}}{a_0}(m) \right) \cos(2t) \\ \sum_{n=1}^{\infty} \left(\frac{a_n}{a_0}(m) - \frac{a_{-n}}{a_0}(m) \right) \sin(2t) \\ 0 \end{pmatrix}, \tag{1}$$

where $a_{-n}(m), \ldots, a_0(m), \ldots a_n(m)$ are coefficients expressed as polynomials in m. These coefficients can be computed up to an arbitrary order in m following Reference 18. In the current work, we only consider the coefficients up to order 6 in m, as in Reference 16. Defining the nondimensional mass of Moon as $\mu = m_2/(m_1 + m_2)$ where m_i is the mass of P_i, the positions of the Earth and Moon in this frame are $\mathbf{r}_1(t) = -\mu \mathbf{r}_{v.o.}(t)$ and $\mathbf{r}_2(t) = (1-\mu)\mathbf{r}_{v.o.}(t)$, respectively. The Sun is located at $\mathbf{r}_0(t)^\top = M^{-1/3} a_0(m) \left(\cos(t), -\sin(t), 0\right)$, where $M = (m_1 + m_2)/m_0$. For the Sun–Earth–Moon system, $\mu = 0.01215$ and $M = 3.0404 \times 10^{-6}$. Note that the model does not account for the inclination of the Earth–Moon orbit relative to the ecliptic, as the orbits of the three celestial bodies are assumed to lie in the $(\hat{\mathbf{e}}_x, \hat{\mathbf{e}}_y)$-plane. However, this assumption is justified, as the actual maximum inclination is approximately 5 degrees.

Denoting the position of the particle P_3 with $\mathbf{r} = (x, y, z)^\top$, its velocity with $\mathbf{v} = (\dot{x}, \dot{y}, \dot{z})^\top$, and its state with $\mathbf{x} = \left(\mathbf{r}^\top, \mathbf{v}^\top\right)^\top$, the HR4BP equations of motion are given by[16]

$$\dot{\mathbf{x}} = \mathbf{f}(\mathbf{x}, t) = \begin{pmatrix} \mathbf{v} \\ \dfrac{\partial V}{\partial \mathbf{r}}(\mathbf{r}, t) + 2(1+m)\mathbf{v} \times \hat{\mathbf{e}}_z \end{pmatrix}, \tag{2}$$

where

$$\begin{aligned} V(\mathbf{r}, t) := \frac{1}{2}\left(1 + 2m + \frac{3}{2}m^2\right)\left(x^2 + y^2\right) - \frac{1}{2}m^2 z^2 + \\ + \frac{3}{4}m^2\left(\left(x^2 - y^2\right)\cos(2t) - 2xy\sin(2t)\right) + \frac{m^2}{a_0(m)^3}\left(\frac{1-\mu}{r_{13}(t)} + \frac{\mu}{r_{23}(t)}\right) \end{aligned} \tag{3}$$

and $r_{i3} = ||\mathbf{r} - \mathbf{r}_i||$ denotes the distance between i-th body and the particle. Provided an initial condition $\mathbf{x}_i \in \mathbb{R}^n$ at a time t_i, the flow of the HR4BP, i.e., the solution of Equation (2) at time t, is indicated with $\mathbf{x}(t) = \boldsymbol{\varphi}(\mathbf{x}_i,\, t_i;\, t)$.

Given that $a_0(m) = m^{2/3}(1 - 2/3m + \mathcal{O}(m^2))$, we see that when $m = 0$, the equations of motion reduce to the CR3BP. In other words, as $m \to 0$, the Sun's influence on the Earth–Moon system is removed. A physical interpretation can be obtained by examining the Sun's position as a function of m. Notice that as $m \to 0$, $||\mathbf{r}_0|| \to \infty$, meaning that as m decreases, the Sun moves farther away from the Earth–Moon system. When $m = 0$, the Sun is at infinity, and when $m = 0.0808$, the Sun is at its actual nominal distance from the Earth–Moon system.

The HR4BP can be interpreted as a periodic perturbation of the Earth–Moon CR3BP, with the perturbing force being π-periodic. As a result, the Sun's influence follows half-month periodicity, a consequence of the symmetry inherited from the Hill approximation. Specifically, under this approximation, the Sun's effect is symmetric around the Earth–Moon barycenter. This invariance,

combined with the fact that the variation orbit repeats every half-month in this frame, leads to the π-periodicity of the equations.

Another notable feature of the HR4BP is that it is a periodic Hamiltonian system, a property that has many important implications, especially for the nature of invariant solutions.[4,5,28,33]

Dynamical Equivalents of Equilibrium Points and Resonant Periodic Orbits

When a time-periodic perturbation is added to an autonomous system, e.g., the CR3BP, a single structure in the autonomous system may have multiple dynamical equivalents (DE) in the perturbed system (i.e., related structures that exist in the perturbed system).[26] Thus, it is convenient to start the search for invariant manifolds in the HR4BP from the known invariant solutions of the CR3BP (see Reference 34 for a detailed overview on the families of CR3BP periodic orbits).

Under the Sun's perturbation, the equilibria (0-dimensional invariant manifolds) of the CR3BP become small π-periodic orbits (1-dimensional invariant manifolds). These periodic orbits are often referred to as the dynamical equivalents or substitutes of the libration points. They are computed through a continuation procedure that starts from the equilibrium points in the CR3BP ($m = 0$). As the parameter m is gradually increased, a multiple-shooting method is applied to compute the periodic orbits that take the place of the equilibrium points.[4,16,23,35] However, during the continuation process bifurcations may be encountered. This is the case of L_2, where a broken pitchfork bifurcation produces multiple dynamical equivalents similar to π-periodic planar Lyapunov orbits. Some dynamical equivalents of L_1 and L_2 are shown in Figure 2.

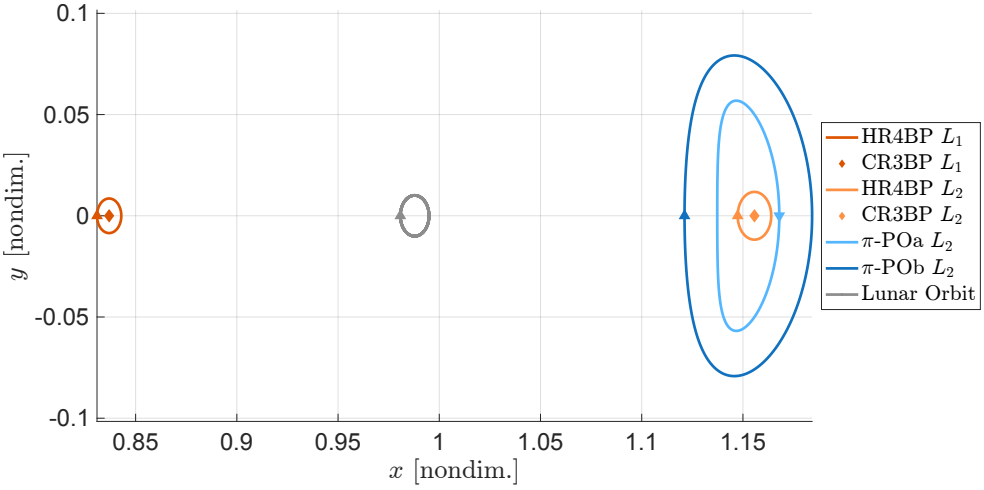

Figure 2. HR4BP dynamical equivalents of L_1 and L_2 together with some π-periodic orbits emanating from a bifurcation during the continuation of L_2; arrows show the direction of motion along the orbits and the positions at initial time $t = 0$; diamond markers indicate the original locations of the equilibria in the CR3BP

Periodic orbits replacing the CR3BP equilibria are not the only periodic solutions of a HR4BP, as CR3BP periodic orbits of a resonant period may persist. In contrast to the CR3BP, where periodic orbits lie in one-parameter families, periodic orbits in the HR4BP exist as isolated solutions. To ensure the periodicity of an orbit in such model, the period of the orbit must be commensurate with the period π of the Sun perturbation. A methodology leveraging Melnikov theory was recently employed for a rigorous search of periodic orbits in the HR4BP.[26]

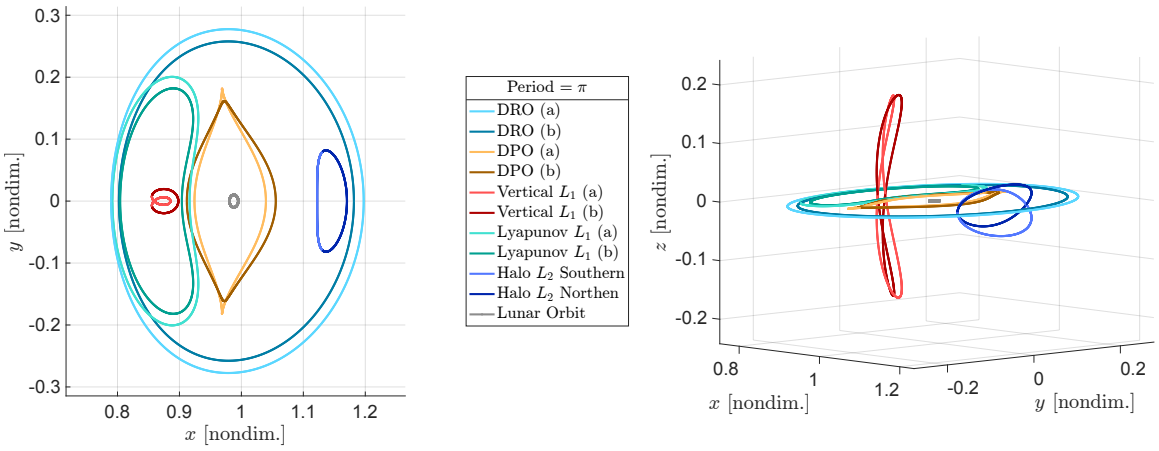

Figure 3. Several π-periodic HR4BP orbits near L_1 and L_2, shown in a top view (left) and a side view (right)

Figure 3 shows several π-periodic orbits in the vicinity of L_1 and L_2, obtained by continuing the corresponding CR3BP orbits from $m = 0$ to $m = 0.0808$. Solutions labeled (a) or (b) originate from the same initial three-body orbit, with the difference arising from the choice of the state on the orbit used as the initial condition at $t = 0$. Additionally, note in Figure 3 the presence of some P_2-centered orbits, such as distant retrograde orbits (DROs) and distant prograde orbits (DPOs), which were not included in Reference 26.

The normal behavior of periodic orbits can be studied through the eigenvalues of their monodromy matrices. The L_1 and L_2 dynamical equivalents exhibit the same normal behavior as the corresponding equilibrium points in the CR3BP. Specifically, there is one out-of-plane center direction (i.e., along $\mathbf{e}_z$), one in-plane center direction, and one in-plane hyperbolic direction. Thus, the orbits are of type center $\times$ center $\times$ saddle. Additionally, π-PO L_2 (a) and π-PO L_2 (b) in Figure 2 share the same stability type. This normal behavior implies the existence of two one-parameter (Cantorian) families of two-dimensional quasi-periodic orbits (one planar and one vertical) as well as two-parameter families of three-dimensional quasi-periodic orbits surrounding each of these periodic orbits. The eigenvectors associated with the center directions will be used to generate initial guesses for the families of quasi-periodic orbits emanating from the periodic orbit. Conversely, when a saddle component is present, hyperbolic manifolds can be computed by perturbing each state of the orbit along the stable and unstable eigenvectors of the monodromy matrix. Figure 4 illustrates the hyperbolic manifolds of the dynamical equivalents of L_1 and L_2, which may prove useful for designing transfer trajectories in the HR4BP.

Invariant Tori

At the heart of a quasi-periodic invariant torus is the fundamental topological structure known as a torus, defined as the Cartesian product of circles. A circle is represented by the set $\mathbb{S}^1 = \mathbb{R}/\mathbb{Z}$, which, for convenience in this work, parametrizes angles on the unit interval. This means angles are considered within the range $[0, 1]$ rather than the more traditional $[0, 2\pi]$. A d-dimensional torus, or d-torus, is then expressed as $\mathbb{T}^d = \mathbb{S}^1 \times \cdots \times \mathbb{S}^1$ (with d instances of $\mathbb{S}^1$). It can be parameterized over its surface by d independent coordinates, $\boldsymbol{\theta} = (\theta_1, \ldots, \theta_d)^\top \in \mathbb{T}^d$. With this parametrization, the angular coordinates satisfy $\boldsymbol{\theta} = \boldsymbol{\theta} + \boldsymbol{k}$ for any $\boldsymbol{k} \in \mathbb{Z}^d$, reflecting the periodic nature of the torus.

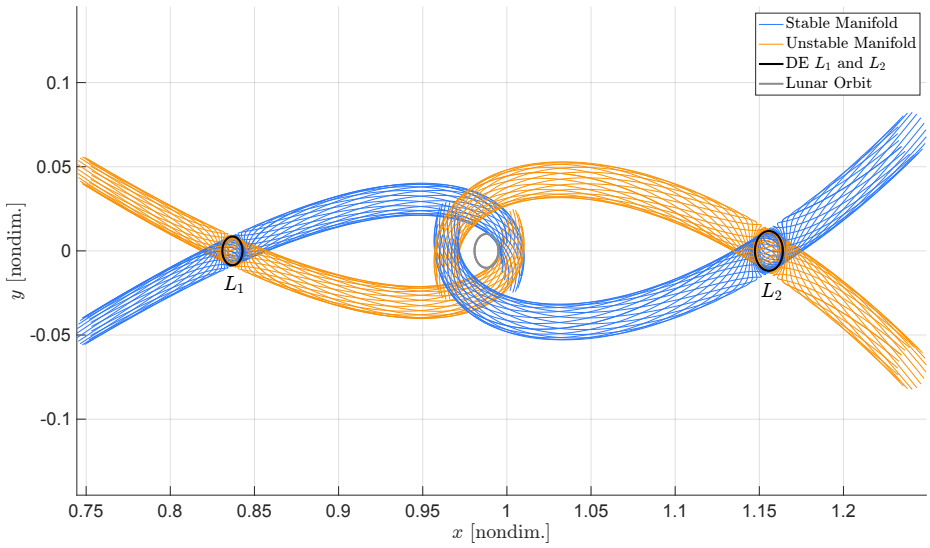

Figure 4. Stable and unstable manifolds emanating from the dynamical equivalents of L1 and L2

A quasi-periodic torus is a special case of a standard torus in which the set of angles $\boldsymbol{\theta}$ are governed by the dynamics $\dot{\boldsymbol{\theta}} = \boldsymbol{\omega}$, with $\dot{\boldsymbol{\omega}} = \mathbf{0}$. The vector $\boldsymbol{\omega} \in \mathbb{R}^d$, known as frequency vector, contains the constant rates at which each angle evolves over time. The flow of a d-dimensional quasi-periodic orbit is analogous to the motion on a quasi-periodic d-torus, which is characterized by d internal frequencies. We assume that the frequency vector is not resonant. In other words, for $\boldsymbol{k} \in \mathbb{Z}^d$, $\boldsymbol{k}^\top \boldsymbol{\omega} = 0$ only if $\boldsymbol{k} = \mathbf{0}$. Over time, a quasi-periodic orbit densely winds around the surface of the torus. Since the closure of the quasi-periodic orbit is an invariant torus, the two terms will be used interchangeably.

In this work, we consider 2-dimensional tori, so $d = 2$ and $\boldsymbol{\theta} = (\theta_1, \theta_2)^\top$. The aim is to represent a quasi-torus in our dynamical system using a diffeomorphism called torus function,

$$\boldsymbol{v}(\theta_1, \theta_2) : \mathbb{T}^1 \times \mathbb{T}^1 \to \mathbb{R}^n, \tag{4}$$

which parametrizes the states on the torus using the angles $\boldsymbol{\theta}$. In the case of the HR4BP, $n = 6$ is the dimension of the phase space. Figure 5 illustrates a 2-dimensional standard torus and the quasi-periodic torus mapped by the torus function.

In order for the torus to be invariant, the motion on the torus must be consistent with the vector field $\mathbf{f}$ of the dynamical system. Substituting the torus function definition into Equation (2), i.e., setting $\mathbf{x} = \boldsymbol{v}(\theta_1, \theta_2)$, gives the invariance equation[28]

$$\omega_1 \frac{\partial \boldsymbol{v}(\theta_1, \theta_2)}{\partial \theta_1} + \omega_2 \frac{\partial \boldsymbol{v}(\theta_1, \theta_2)}{\partial \theta_2} = \mathbf{f}(\boldsymbol{v}(\theta_1, \theta_2), t). \tag{5}$$

In other words, as the vector field $\mathbf{f}$ is a linear combination of $\partial \boldsymbol{v}/\partial \theta_1$ and $\partial \boldsymbol{v}/\partial \theta_2$, it must be tangent to the torus surface.

Since the HR4BP is a periodically forced system, one of the frequencies of each quasi-periodic orbit must correspond to the frequency of the external perturbation.[5] We designate the first frequency ω_1 as the perturbation frequency. Consequently, θ_1 will appear explicitly in the vector field and serve as the time parameter.

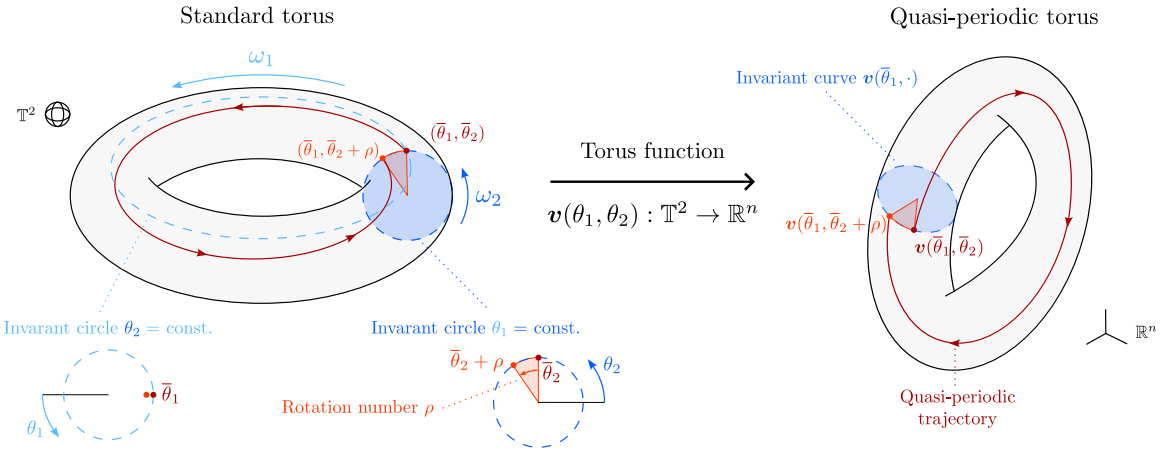

Figure 5. Illustration of a standard 2-torus (left) and a two-dimensional quasi-periodic torus in $\mathbb{R}^n$ (right) mapped by the diffeomorphism $\boldsymbol{v}$; the effect of a stroboscopic mapping with period T_1 is shown on both manifolds

To ensure consistency with the unit interval parametrization of the angles, we rescale nondimensional time t as $\tau := t/T$, where $T = \pi$ is the period of the external perturbation of the HR4BP. The rescaling implies that $T_1 = 1$ (mod. 1) and $\omega_1 = 1/T_1 = 1$ (mod. 1).

Yet, instead of looking for a parametrization of $\boldsymbol{v}(\theta_1, \theta_2)$, we reduce the dimension of the problem by looking at a curve on the torus with $\theta_1 \equiv \tau =$ constant. Indeed, if we consider a stroboscopic map associated to the period T_1 of the external perturbation, fixing an initial value $\overline{\theta}_1$ for θ_1, and integrating the flow for $\Delta\tau = T_1$ (or $\Delta t = T$) leaves $\theta_1 = \overline{\theta}_1 + 1 = \overline{\theta}_1$ unchanged and gives $\theta_2 = \overline{\theta}_2 + \rho$, where $\rho = T_1\omega_2 = \omega_2/\omega_1$ is the rotation number. From the assumption that ω_1 and ω_2 are not resonant, ρ is irrational.

Let the flow map induced by $\mathbf{f}$ after T_1 time units be indicated with $\boldsymbol{\varphi}_{T_1}(\tau)$. The problem now becomes finding an invariant curve (one-dimensional invariant torus) described by the circle function $\boldsymbol{w}(\cdot) := \boldsymbol{v}(\theta_1, \cdot) : \mathbb{T}^1 \to \mathbb{R}^n$. The invariance equation for the circle function is

$$\boldsymbol{w}(\theta_2 + \rho) = \boldsymbol{\varphi}_{T_1}(\boldsymbol{w}(\theta_2)). \tag{6}$$

Figure 5 illustrates two invariant circles of a 2-torus, obtained by fixing one angle while allowing the other to vary (blue and light-blue circles at the bottom-left of the picture). Additionally, an invariant curve of the quasi-periodic torus and the angular shift induced by the stroboscopic map are depicted on the right (in blue and orange, respectively).

METHODOLOGY

The methodology described, originally introduced in Reference 28, enables the parametrization of two-dimensional tori by combining Fourier discretization with Gauss–Legendre collocation. By leveraging Newton algorithm to solve the discretized equations, the method is designed to maximize the sparsity of the associated Jacobian matrix, ensuring both computational efficiency and robustness, as detailed in Reference 27. In the following section, this method is adapted to compute two-dimensional invariant tori in the HR4BP starting from periodic orbits.

Cylinder Function

To set up a parametrization that can be easily adapted to a collocation method, we do not consider a single circle function $\boldsymbol{w}(\cdot)$, but instead we define a cylinder function

$$\boldsymbol{u}(\tau;\theta_2) : [0,1] \times \mathbb{T}^1 \to \mathbb{R}^n, \tag{7}$$

where θ_2 is now intended as a parameter. The cylinder function has a dual interpretation. It can be viewed as a set of circle functions $\boldsymbol{u}(\tau;\cdot) = \boldsymbol{w}(\cdot) : \mathbb{T}^1 \to \mathbb{R}^n$, parameterized by the normalized time $\tau \in [0,1]$ along the flow. Alternatively, it can represent a set of trajectories originating from an initial circle function $\boldsymbol{u}(0;\cdot)$. Indeed, for a given $\theta_2 = \overline{\theta}_2$, $\boldsymbol{u}(\cdot\,;\overline{\theta}_2)$ represents an individual trajectory with initial condition $\boldsymbol{u}(0;\overline{\theta}_2)$. In other words, the function $\boldsymbol{u}$ is defined such that θ_2 corresponds to the angle on the initial invariant circle, and it is constant along a given trajectory. Both interpretations will prove useful in the computational scheme.

The torus and cylinder functions are related by:

$$\boldsymbol{v}(\theta_1,\theta_2) = \boldsymbol{u}(\tau;\theta_2 - \rho\tau), \quad \text{where } \tau \equiv \theta_1. \tag{8}$$

Indeed, by identifying the two ends of the cylinder, it can be topologically transformed into a torus. A sketch of the cylinder function is illustrated in Figure 6.

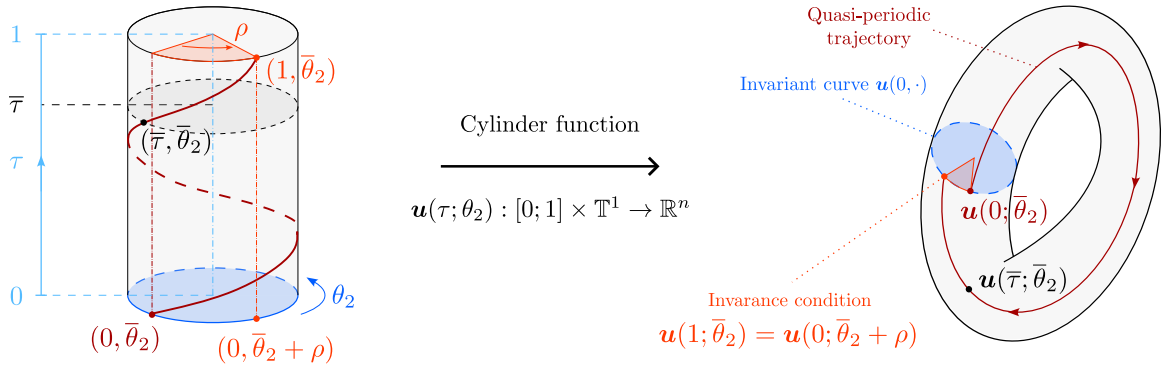

Figure 6. Illustration of a cylinder function for a two-dimensional quasi-periodic invariant torus

Recalling that the stroboscopic map $\boldsymbol{\varphi}_{T_1}$ generates a shift equal to ρ in θ_2 while τ progresses from 0 to 1, the invariance condition for the cylinder function can be expressed as:

$$\boldsymbol{u}(0;\theta_2) = \boldsymbol{u}(1;\theta_2 - \rho). \tag{9}$$

Following Reference 28, an augmented vector field $\mathbf{f}_a$ is introduced to express the motion that each quasi-periodic trajectory departing from the initial invariant curve must follow. The dynamics for the cylinder function is written as

$$\frac{1}{T}\frac{\mathrm{d}\boldsymbol{u}}{\mathrm{d}\tau}(\tau;\theta_2) = \mathbf{f}_a(\boldsymbol{u}(\tau;\theta_2),\tau,\theta_2;\lambda), \tag{10}$$

where the factor $1/T$ accounts for the unitary normalization of the time variable τ. Recall that the HR4BP a periodically forced system with the angle $\theta_1 \equiv \tau$ explicitly appearing in the equations of motion. As a consequence, the augmented vector field $\mathbf{f}_a$ takes the form:

$$\mathbf{f}_a(\mathbf{u}(\tau;\theta_2),\tau,\theta_2;\lambda) := \mathbf{f}(\mathbf{u}(\tau;\theta_2),\tau) + \lambda\,\mathbf{J}\frac{\partial \mathbf{u}(\tau;\theta_2)}{\partial\theta_2}\bigg|_{(\tau,\theta_2)}, \tag{11}$$

where λ, referred to as the unfolding parameter, modifies the dynamics but does not affect the structure of a quasi-periodic solution. Additional details can be found in Reference 28. Considering λ as an free variable will ensure that the number of unknowns matches the number of constraints, which is advantageous for the numerical computation of a solution. In Equation (11), $\mathbf{J}$ is a constant matrix associated with the gradient a local integral of motion (the torus action I_2 related to the angle θ_2). In the present case, the matrix $\mathbf{J}$ is given by:

$$\mathbf{J} = \left[\begin{array}{ccc|ccc} & +\widetilde{m} & & -1 & & \\ -\widetilde{m} & & & & -1 & \\ & & & & & -1 \\ \hline +1 & & & & & \\ & +1 & & & & \\ & & +1 & & & \end{array}\right], \quad \text{where } \widetilde{m} = 2(m+1). \tag{12}$$

Torus Discretization

To compute the cylinder function $\boldsymbol{u}(\tau;\theta_2)$, we adopt a two-step discretization approach. First, the second argument is discretized by restricting the angle θ_2 to a set of evenly spaced values, used to approximate each invariant curve $\boldsymbol{u}(\tau;\cdot)$ with a truncated Fourier series. Next, the resulting set of trajectories on the torus surface is discretized in time using continuous piecewise polynomials, with the vector field enforced at some collocation points.

As previously noted, the cylinder function can be interpreted as a collection of circle functions, $\boldsymbol{u}(\tau;\cdot) : \mathbb{T}^1 \to \mathbb{R}^n$, defined at different normalized times $\tau \in [0,1]$ along the flow. Each circle function is approximated by a Fourier series truncated at a prescribed order M_F:

$$\boldsymbol{u}(\tau;\theta_2) = \sum_{|k|\leq M_F} \boldsymbol{c}_k(\tau)\, e^{ik(2\pi\theta_2)}, \tag{13}$$

where $k \in \mathbb{Z}$ is the Fourier index, and $\boldsymbol{c}_k(\tau) \in \mathbb{C}^n$ are the Fourier coefficients.

The discrete Fourier transform (DFT) is a linear and invertible operation used to establish the relationship between the $N_F = 2M_F + 1$ Fourier coefficients $\{\boldsymbol{c}_k(\tau)\}$ and the N_F states $\{\boldsymbol{u}(\tau; k/N_F)\}$ that belong to the curve (see References 10 and 32 for further details on the DFT operator). The discretized circle function at time τ can thus be fully represented by the set of states corresponding to the evenly spaced angle $\theta_2^{(k)} = k/N_F$. Accordingly, a collected state vector is introduced

$$\mathbf{X}(\tau) := \left\{ \mathbf{x}^{(k)}(\tau) = \boldsymbol{u}\left(\tau; \frac{k}{N_F}\right) \;\middle|\; k = 0, \ldots, N_F - 1 \right\}. \tag{14}$$

Similarly, the collected vector field is defined as:

$$\mathbf{F}(\mathbf{X}(\tau), \tau; \lambda) := \left\{ \mathbf{f}_a\left(\mathbf{x}^{(k)}(\tau), \tau, \frac{k}{N_F} + \rho\tau; \lambda\right) \;\middle|\; k = 0, \ldots, N_F - 1 \right\}. \tag{15}$$

Both $\mathbf{X}(\tau)$ and $\mathbf{F}(\mathbf{X}(\tau), \tau; \lambda)$ belong to $\mathbb{R}^{n^*}$, where $n^* = nN_F$.

The dynamics of the cylinder function, Equation (10), can be written in terms of the collected state and vector field as

$$\frac{\mathrm{d}\mathbf{X}}{\mathrm{d}\tau}(\tau) = T\mathbf{F}(\mathbf{X}(\tau), \tau; \lambda). \tag{16}$$

The quasi-periodic boundary condition in Equation (9) becomes

$$\mathbf{X}(0) = \mathbf{R}(-\rho)\mathbf{X}(1), \tag{17}$$

where the real $n^* \times n^*$ rotation matrix $\mathbf{R}(-\rho)$ can be constructed by the composition of the DFT matrix, the phase shift $-\rho$, and the inverse DFT matrix.

The N_F states on each circle function can be viewed as N_F trajectories as time flows. Each individual trajectory, $\mathbf{x}^{(k)}(\cdot)$, is approximated as a continuous piecewise polynomial of degree M across N time intervals, separated by $N+1$ evenly spaced nodes:

$$0 = \tau_{0,0} < \tau_{1,0} < \cdots < \tau_{N,0} = 1.$$

Within each interval, M collocation points are chosen as the roots of the Mth degree Legendre polynomial, $\{\hat{\tau}_1, \ldots, \hat{\tau}_M\}$, appositely rescaled from the interval $(-1, 1)$ to $(0, 1)$. This process constructs a time grid, $\{\tau_{i,j}, \tau_{N,0}\}$, where $i = 0, \ldots, N-1$ and $j = 0, \ldots, M$. When sampled on the time grid, the collected vector $\mathbf{X}(\tau)$ is denoted as $\mathbf{X}_{i,j}$. Within the i-th interval, for $\tau \in [\tau_{i,0}, \tau_{i+1,0}]$, quasi-periodic orbits are expressed as

$$\mathbf{X}(\tau) = \sum_{j=0}^{M} \mathbf{X}_{i,j}\ell_j(\hat{\tau}), \quad \text{where} \quad \hat{\tau} = \frac{\tau - \tau_{i,0}}{\tau_{i+1,0} - \tau_{i,0}}, \tag{18}$$

and $\ell_j(\hat{\tau})$ is the Lagrange basis polynomial:

$$\ell_j(\hat{\tau}) = \prod_{\substack{m=0 \\ m \neq j}}^{M} \frac{\hat{\tau} - \hat{\tau}_m}{\hat{\tau}_j - \hat{\tau}_m}. \tag{19}$$

The Lagrange basis polynomials satisfy the property $\ell_j(\hat{\tau}_m) = \delta_{j,m}$, where δ is the Kronecker delta. The variable $\hat{\tau}$ rescales the time $\tau \in [\tau_{i,0}, \tau_{i+1,0}]$ to the interval $[0, 1]$, where the roots of the Legendre polynomials are defined.

A pictorial representation of the torus discretization is shown in Figure 7. On the top left, the time grid (or equivalently θ_1-grid) is represented by light-blue crosses at the nodes, while black diamond markers indicate the collocation points within each interval. The timeline is depicted as a circle to emphasize periodicity, recalling that the cylinder function describes a torus by identifying the two ends at $\tau_{0,0}$ and $\tau_{N,0}$. The Fourier discretization of the initial invariant curve (shown in blue) is included at the bottom left, along with the angular shift ρ caused by the stroboscopic mapping. At the center, the discrete circle functions $\mathbf{X}_{i,0}$ at the time grid nodes are depicted in dark red, while black is used to distinguish the collocation states $\mathbf{X}_{i,j}$. On the right, an enlarged view illustrates how the collocation method aligns the polynomial trajectory with the local augmented vector field, depicted by arrows.

Continuity is enforced between the piecewise polynomials at the times $\tau_{i,0}$ through

$$\sum_{j=0}^{M} \mathbf{X}_{i,j}\ell_j(1) = \mathbf{X}_{i+1,0}, \quad \text{for } i = 0, \ldots, N-1. \tag{20}$$

In the Gauss–Legendre collocation method, instead of integrating the dynamics, we require the derivative of the piecewise polynomial $\mathbf{X}(\tau)$ to match the vector field $\mathbf{F}$ at the collocation points.

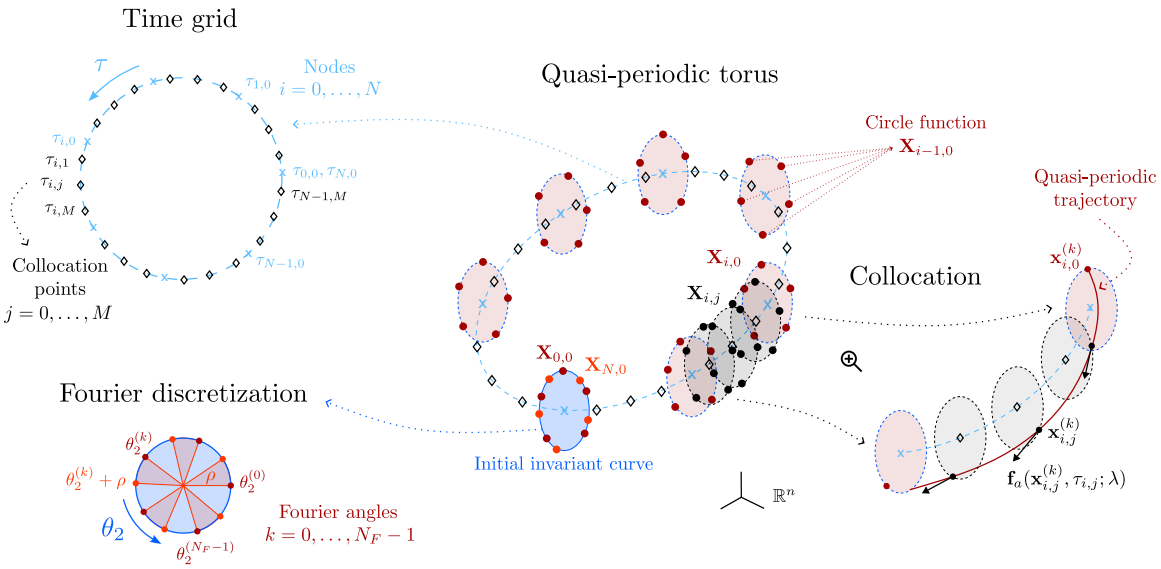

Figure 7. Pictorial representation of the two discretization levels used for the quasi-periodic torus: one involving time, and the other the invariant curves

Thus, Equation (16) is replaced by the following set of $N \times M \times n^*$ constraints

$$\sum_{m=0}^{M} \mathbf{X}_{i,m} \frac{\mathrm{d}\ell_m}{\mathrm{d}\hat{\tau}}(\hat{\tau}_j) = \frac{T}{N}\mathbf{F}(\mathbf{X}(\tau_{i,j}), \tau_{i,j}; \lambda), \qquad \begin{matrix} i = 0, \ldots, N-1 \\ j = 1, \ldots, M \end{matrix} \quad , \tag{21}$$

where it is used $\mathrm{d}/\mathrm{d}\tau = \mathrm{d}/\mathrm{d}\hat{\tau} \cdot \mathrm{d}\hat{\tau}/\mathrm{d}\tau = \mathrm{d}/\mathrm{d}\hat{\tau} \cdot 1/(\tau_{i+1,0} - \tau_{i,0}) = \mathrm{d}/\mathrm{d}\hat{\tau} \cdot N$.

Additional n^* scalar constraints are provided by the quasi-periodic condition applied to the N_F states on the initial and final invariant curves. Equation (17) is rewritten as:

$$\mathbf{X}_{0,0} = \mathbf{R}(-\rho)\mathbf{X}_{N,0}. \tag{22}$$

To simplify notation, the states discretizing the torus are grouped into a vector $\mathbf{X} \in \mathbb{R}^{(n^*N(M+1)+n^*)}$

$$\mathbf{X} = \left(\mathbf{X}_{i,j}{}^{\top}, \mathbf{X}_{N,0}{}^{\top}\right)^{\top}, \quad \text{with} \quad \begin{matrix} i = 0, \ldots, N-1 \\ j = 0, \ldots, M \end{matrix} \quad . \tag{23}$$

Quasi-Periodic Boundary Value Problem

Being the HR4BP a periodic perturbation of an autonomous Hamiltonian system, two-dimensional quasi-periodic tori lie in one-parameter (Cantorian) families.[5] Incorporating pseudo-arclength continuation enables the computation of a single member from each family. A solution is determined by solving a boundary value problem, then the predictor-corrector approach proposed in Reference 36 is used to continue along the family branches.

Such a method is effective only if each member has a unique cylinder function representation. Since any phase shift along θ_2 of the invariant curve also satisfies the boundary conditions, an additional phase constraint is required to anchor the solution. In this work, we adopt a phase condition that minimizes the phase difference between the current curve and a previously computed curve.[10,23,24] This introduces an additional scalar constraint on the discretized initial invariant

curve $\mathbf{X}_{0,0}$, ensuring its alignment with a previously computed invariant curve of a nearby torus in the family, represented by $\widetilde{\mathbf{X}}_{0,0}$. The phase condition is expressed as:

$$\left(\mathbf{X}_{0,0} - \widetilde{\mathbf{X}}_{0,0}\right)^\top \frac{\partial \widetilde{\mathbf{X}}_{0,0}}{\partial \theta_2} = 0, \tag{24}$$

where the partial derivative with respect to the angle θ_2 is computed using DFT operations.

Let collect the unknowns of the problem in a single vector $\mathbf{Y} \in \mathbb{R}^{N_Y}$, where its dimension is $N_Y = (n^* N(M+1) + n^* + 2)$,

$$\mathbf{Y} := \left(\mathbf{X}^\top, \rho, \lambda\right)^\top. \tag{25}$$

Pseudo-arclength continuation is used to move along the family branch, setting the distance between the current and previous torus at Δs.[36] The resulting constraint is

$$\frac{1}{N_1 N_F}\left(\mathbf{X} - \widetilde{\mathbf{X}}\right)^\top \widetilde{\mathbf{X}}' + (\rho - \widetilde{\rho})\,\widetilde{\rho}' - \Delta s = 0, \tag{26}$$

where $N_1 = N(M+1)+1$ represents the size of the time grid. The distance is defined as the difference projected onto an approximate tangent $\mathbf{Y}' = (\mathbf{X}'^\top, \rho', \lambda')^\top$ evaluated at the previous computed solution $\widetilde{\mathbf{Y}} = (\widetilde{\mathbf{X}}^\top, \widetilde{\rho}, \widetilde{\lambda})^\top$.

A constraint function $\mathbf{H}(\cdot) : \mathbb{R}^{N_Y} \to \mathbb{R}^{N_Y}$ is introduced to encapsulate all the constraints: continuity, collocation, quasi-periodicity, phase, and pseudo-arclength. The Jacobian of $\mathbf{H}(\mathbf{Y})$ with respect to the unknowns, denoted as $\mathrm{D}\mathbf{H}(\mathbf{Y})$, can be computed analytically, though the expression is omitted here for the sake of conciseness.

The family tangent used in the pseudo-arclength discretization can be extracted from the null space of the Jacobian of the constraint, after removing the column corresponding to λ and the row corresponding to the collocation constraint. The one-dimensional null space of the reduced Jacobian is then normalized such that

$$\frac{1}{N_1 N_F}\widetilde{\mathbf{X}'}^\top \widetilde{\mathbf{X}'} + \widetilde{\rho'}^2 = 1. \tag{27}$$

Bifurcations are identified when the size of the null space increases. Moreover, the flipping condition introduced by Reference 37 is used to track previously determined path orientation and ensure the continuous following of the same direction.

Predictor-Corrector Scheme

To initialize the computation of a family of quasi-periodic orbits, a guess for the initial invariant curve is required. This is computed through a linear approximation based on the eigenvectors of the monodromy matrix of the underlying periodic orbits in the HR4BP. Specifically, the eigenvector $\mathbf{v}_\lambda$ associated with a complex unitary eigenvalue is used[23]

$$\mathbf{u}^{(0)}(0;\theta_2) = \mathrm{Re}[\mathbf{v}_\lambda]\cos(2\pi\theta_2) - \mathrm{Im}[\mathbf{v}_\lambda]\sin(2\pi\theta_2). \tag{28}$$

The rotation number is estimated as $\rho^{(0)} = \tan^{-1}(\lambda_I/\lambda_R)$, where λ_I and λ_R represent the imaginary and real parts of the central eigenvalue, respectively.

Once an initial guess is obtained, pseudo-arclength continuation can be efficiently applied. The predictor step estimates the next solution starting from the previous one (except for the first iteration,

where Equation (28) is used as the predictor):

$$\mathbf{Y}^{(0)} = \left(\widetilde{\mathbf{X}}^{\top} + \Delta s \widetilde{\mathbf{X}'}^{\top}, \widetilde{\rho} + \Delta s \widetilde{\rho'}, \widetilde{\lambda}\right)^{\top}. \tag{29}$$

Subsequently, the corrector step is performed using a Newton method, iterating until $||\mathbf{H}(\mathbf{Y})||$ is below a fixed tolerance, set to 10^{-12}. The n-th Newton iteration is

$$\mathbf{Y}^{(n)} = \mathbf{Y}^{(n-1)} + \mathrm{D}\mathbf{H}\left(\mathbf{Y}^{(n-1)}\right)^{-1} \mathbf{H}\left(\mathbf{Y}^{(n-1)}\right). \tag{30}$$

Notably, the inclusion of the unfolding parameter λ ensures a system with an equal number of equations and unknowns, resulting in a square Jacobian $\mathrm{D}\mathbf{H}$. This enables the use of a standard Newton method for solving the discretized equations, which is more computationally efficient than, for instance, using a pseudo-inverse (as in a Gauss–Newton method). Gauss–Legendre collocation produces a notably sparse Jacobian matrix, allowing for effective sparse LU factorization during Newton iterations. Furthermore, as the unfolding parameter λ is exponentially small, terms of $\mathcal{O}(\lambda)$ can be omitted from the Jacobian $\partial \mathbf{f}_a / \partial \mathbf{X}_{i,j}$ of the collocation constraint without affecting convergence while significantly increasing sparsity.[28] Figure 8 provides an example of the sparsity pattern of the Jacobian matrix.

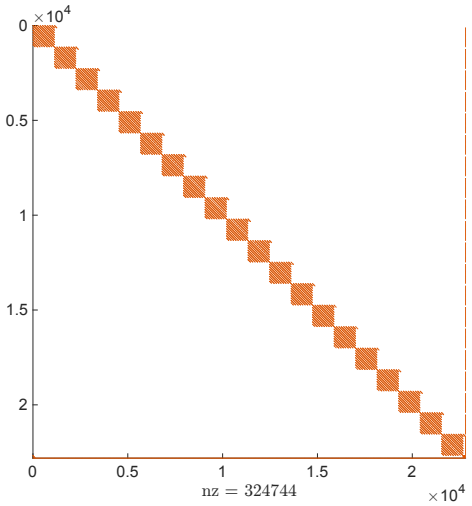

Figure 8. Sparsity of Jacobian matrix $\mathrm{D}\mathbf{H}$, with $N = 20$ intervals, Lagrange degree $M = 8$, and Fourier Order $M_F = 10$

Discretization Error Control

Even when the constraints are satisfied (i.e., $\|\mathbf{H}(\mathbf{Y})\| < 10^{-12}$), there is no guarantee that $\mathbf{X}_{0,0}$ accurately represents an invariant curve $\boldsymbol{u}(0, \theta_2)$, as the accuracy also depends on the discretization method. Specifically, the convergence of Newton's method only ensures that the invariant constraints are satisfied at the sampling points. Therefore, it is essential to verify whether the accuracy of the Fourier approximation is maintained beyond the N_F trajectories.

The error associated with the collocation is controlled by adjusting the degree of the piecewise polynomial (M) and the number of time intervals (N). These parameters are typically fixed for each family, with $N = 20$ and $M = 7$.

On the other hand, the convergence of the Newton method depends on how accurately the invariant curve is represented by the truncated Fourier series. If the Fourier order M_F is too low, the Newton method may fail to achieve the desired tolerance or may require an excessive number of iterations. In this work, the number of sampling points is not fixed throughout the continuation process. After each corrector step, the invariance condition is tested over a finer grid of points along the invariant curve. Each point is first rotated around θ_2 by $-\rho$ using DFT and then propagated under the original HR4BP flow for $T = \pi$. If the average error between the rotated points and their propagated counterparts exceeds a specified tolerance, the number of Fourier modes (N_F) used to discretize the invariant curve is increased by 5. In general, as the invariant torus becomes more complex, distorted, or larger, a higher Fourier order is required. If, during the continuation process, the Fourier order increases more than 10 times between two solutions, or if the Newton method fails to converge within a reasonable number of iterations, the step size Δs is reduced. The initial value of N_F is set to 10.

Stability of Quasi-Periodic Tori

The linear stability near a computed quasi-periodic invariant torus is addressed using the approach detailed in Reference 28. Specifically, the focus is on identifying the stable and unstable manifolds linked to hyperbolic tori.

The method assumes the tori are reducible.[38] Thus, stability information, including the eigenvalues of the Floquet matrix, is directly obtained from the Jacobian $\mathrm{D}\mathbf{H}$ used in the collocation method. Unstable eigenvectors are first computed for the initial invariant curve and then propagated across the entire torus through the flow. By perturbing the torus along these directions and integrating both forwards and backwards in time, we can numerically construct the hyperbolic manifolds.

RESULTS

The methodology is applied to compute two-dimensional invariant tori in the HR4BP. The families are initialized with an invariant curve derived from a linear approximation of the center manifold of a periodic orbit, and then extended through pseudo-arclength continuation.

Families are generated from both planar and vertical (or out-of-plane) center manifolds associated with the dynamical equivalents of the Lagrangian points L_1 and L_2 (see Figure 2). For each center component, corresponding to a pair of unitary complex conjugate eigenvalues of the monodromy matrix, a one-parameter family of quasi-periodic orbits is computed. Each 2-torus is characterized by a fixed external frequency, with a period $T = 1$ determined by the external perturbation, and a second period, T/ρ, that varies along the family. For clarity, in the following section, we recover the original time units of the HR4BP. Therefore, $T_1 = \pi$ corresponds to half a synodic month, and $T_2 = T_1/\rho = \pi/\rho$.

Figure 9 shows several invariant curves (with $\tau = \theta_1 = 0$ and varying θ_2) from the planar families of 2-tori near the dynamical equivalents of L_1 and L_2. Figure 10 presents examples of quasi-periodic orbits extracted from the family around L_1. Notably, the invariant curves closely resemble planar Lyapunov orbits from the CR3BP.

The planar family at L_1 is bounded by the π-periodic Lyapunov orbits shown in Figure 2. Concerning L_2, the planar family is constrained by a 1:1 resonance, with T_2 approaching π. The last orbits computed are confined to a small region of nearly-resonant behavior, originating from the

π-periodic orbits (a) and (b) shown in Figure 2, as outlined in Reference 35. Figure 11 illustrates the invariant curves of a vertical family around L_1, with a similar structure observed near L_2.

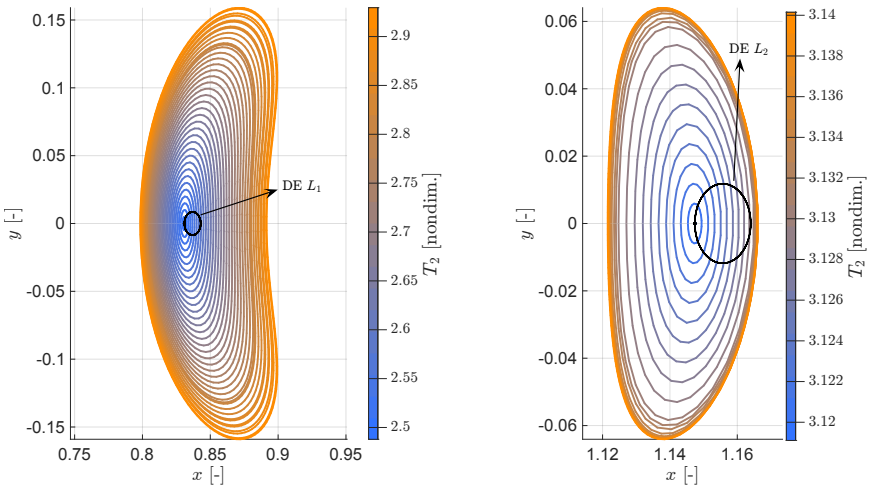

Figure 9. Invariant curves with $\tau = \theta_1 = 0$ of the planar quasi-Lyapunov orbit families around L_1 (left) and L_2 (right)

During the computation of the planar family around L_1, a bifurcation is encountered that leads to the northern and southern families of quasi-halo orbits (see Reference 23 for further details). The invariant curves of the northern halo family are presented in Figure 12, while Figure 13 showcases examples of quasi-halo orbits.

Quasi-halo orbits around L_2 (illustrated in Figures 12 and 13) are computed directly from the center manifold of the resonant π-periodic northern halo orbit shown in Figure 3. According to Reference 23, other families of quasi-halo orbits are expected to bifurcate, but they will be the subject of future studies.

The methodology outlined is also used to calculate quasi-DRO orbits in the HR4BP. Figure 16 shows quasi-DRO orbits originating from a planar center of a DRO π-periodic orbit, while Figure 17 depicts a 2-torus from the vertical family.

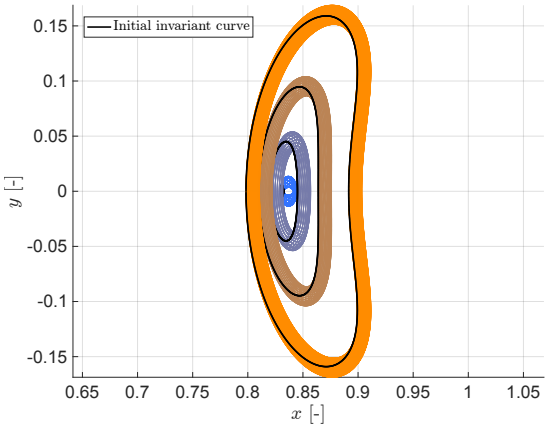

Figure 10. Quasi-Lyapunov orbits at L_1

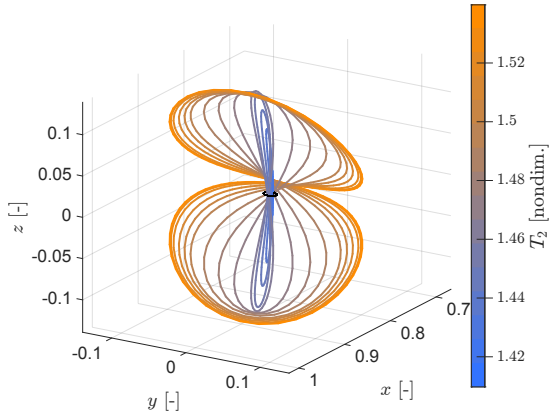

Figure 11. Vertical invariant curves at L_1

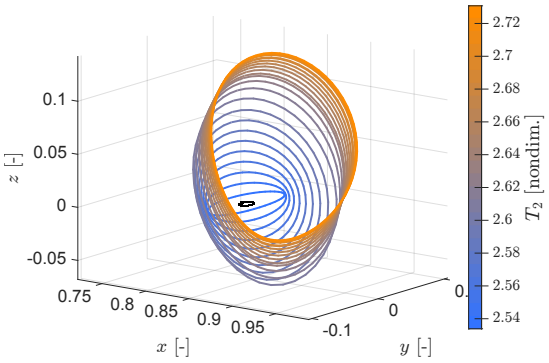

Figure 12. Quasi-halo invariant curves at L_1

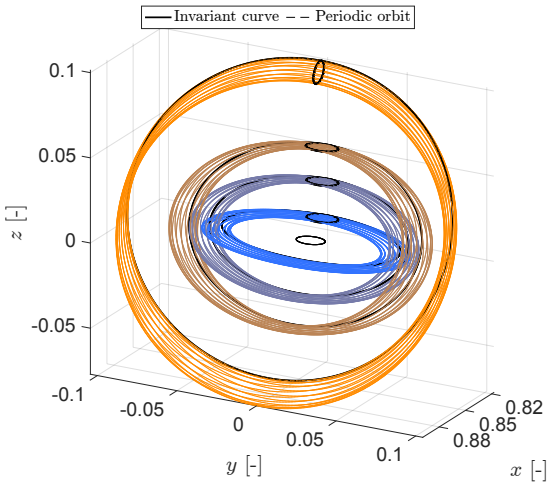

Figure 13. Quasi-halo orbits at L_1

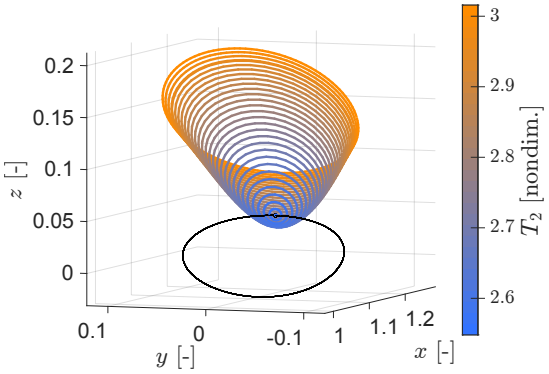

Figure 14. Quasi-halo invariant curves at L_2

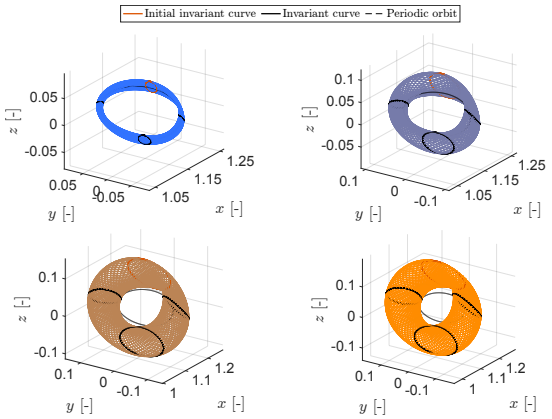

Figure 15. Quasi-halo orbits at L_2

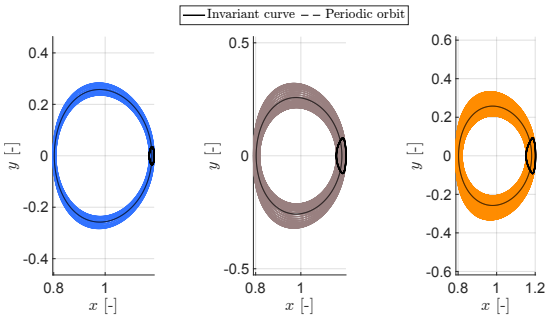

Figure 16. Planar quasi-DROs

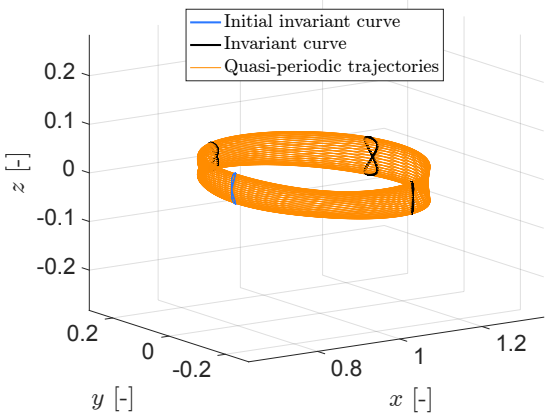

Figure 17. Vertical quasi-DRO

Finally, the stable and unstable manifolds of a quasi-halo orbit are shown in Figure 18. Only the trajectories on the manifolds of two invariant curves are depicted to better understand the geometry. If the entire 2-torus is propagated for a certain period, its image remains a 2-torus, as shown by the cluster of points in Figure 18.

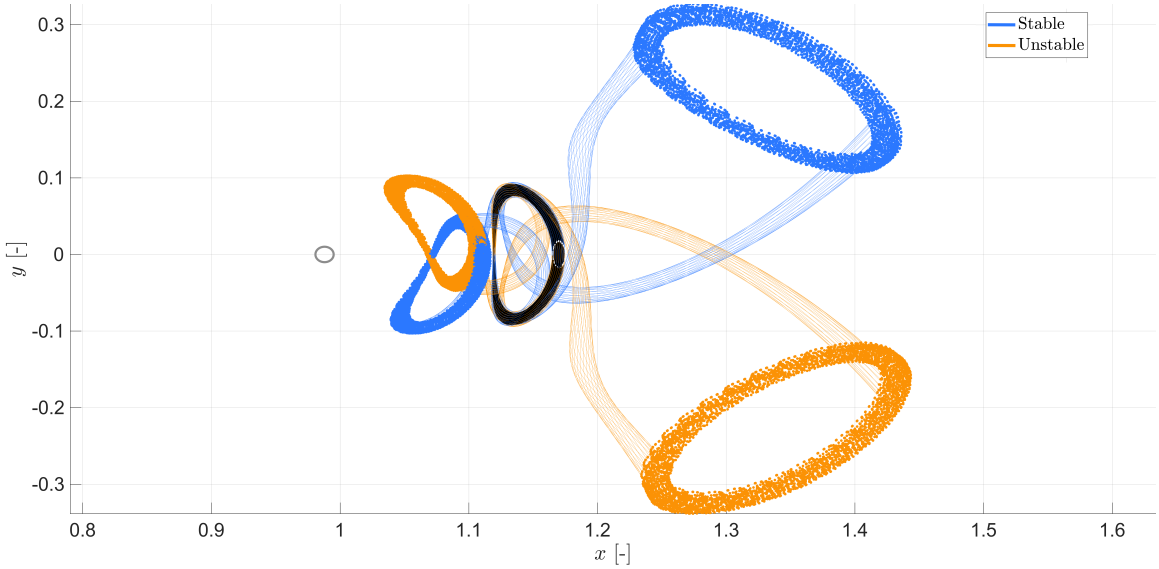

Figure 18. Quasi-halo orbit (in black) with stable and unstable manifolds emanating from two invariant curves; four clusters of points represent the images of the 2-torus along the hyperbolic directions

CONCLUSIONS

In this work, a collocation version of the GMOS algorithm was employed to compute quasi-periodic invariant tori and their associated hyperbolic manifolds in the HR4BP. The methodology leverages pseudo-arclength continuation to compute families of orbits and track the emergence of new branches from bifurcations. Unlike previous studies that computed 2-dimensional tori starting from dynamical equivalents of the Lagrangian points, this approach also incorporates resonant periodic orbits in the HR4BP as initial conditions, such as DROs and halo orbits. This extension allows for a more comprehensive exploration of the dynamics in the Earth–Moon system, particularly in regions away from Lagrangian points.

Future work should focus on the detection and analysis of dynamical boundaries of invariant tori. Identifying these boundaries will be crucial for understanding the stability and transitions between different dynamical regimes. Furthermore, the methodology could be expanded to compute higher-dimensional tori, which would provide an even richer description of the system dynamics and potentially reveal new dynamical features.

Ultimately, a comprehensive understanding of quasi-periodic motion in the HR4BP could significantly expand the possibilities for mission planning, offering new opportunities for exploring and utilizing the Earth–Moon system.

REFERENCES

[1] D. A. Dei Tos and F. Topputo, "On the advantages of exploiting the hierarchical structure of astrodynamical models," *Acta Astronautica*, Vol. 136, jul 2017, pp. 236–247, doi: 10.1016/j.actaastro.2017.02.025.

[2] G. Gómez, J. J. Masdemont, and J. M. Mondelo, "Solar system models with a selected set of frequencies," *Astronomy & Astrophysics*, Vol. 390, July 2002, pp. 733–749, doi: 10.1051/0004-6361:20020625.

[3] V. Szebehely, *Theory of Orbit*. Elsevier, 1967, doi: 10.1016/b978-0-12-395732-0.x5001-6.

[4] L. T. Peterson, J. J. Rosales, and D. J. Scheeres, "The vicinity of Earth–Moon L1 and L2 in the Hill restricted 4-body problem," *Physica D: Nonlinear Phenomena*, Vol. 455, Dec. 2023, p. 133889, doi: 10.1016/j.physd.2023.133889.

[5] Á. Jorba and J. Villanueva, "On the Persistence of Lower Dimensional Invariant Tori under Quasi-Periodic Perturbations," *Journal of Nonlinear Science*, Vol. 7, No. 5, 1997, pp. 427–473, doi: 10.1007/s003329900036.

[6] S. Huang, "Very restricted four-body problem," *Publications of Goddard Space Flight Center*, Vol. 354, 1960.

[7] Á. Jorba, M. Jorba-Cuscó, and J. J. Rosales, "The vicinity of the Earth–Moon L1 point in the bicircular problem," *Celestial Mechanics and Dynamical Astronomy*, Vol. 132, Feb. 2020, doi: 10.1007/s10569-019-9940-2.

[8] B. Le Bihan, J. J. Masdemont, G. Gómez, and S. Lizy-Destrez, "Invariant manifolds of a non-autonomous quasi-bicircular problem computed via the parameterization method," *Nonlinearity*, Vol. 30, June 2017, pp. 3040–3075, doi: 10.1088/1361-6544/aa7737.

[9] J. J. Rosales, Á. Jorba, and M. Jorba-Cuscó, "Families of Halo-like invariant tori around L2 in the Earth-Moon Bicircular Problem," *Celestial Mechanics and Dynamical Astronomy*, Vol. 133, Mar. 2021, doi: 10.1007/s10569-021-10012-0.

[10] B. P. McCarthy and K. C. Howell, "Leveraging quasi-periodic orbits for trajectory design in cislunar space," *Astrodynamics*, Vol. 5, Jan. 2021, pp. 139–165, doi: 10.1007/s42064-020-0094-5.

[11] M. A. Andreu, *The Quasi-Bicircular Problem*. Phd thesis, Departament de Matematica Aplicada i Analisi, Universitat de Barcelona, 1998.

[12] J. J. Rosales, Á. Jorba, and M. Jorba-Cuscó, "Invariant manifolds near L1 and L2 in the quasi-bicircular problem," *Celestial Mechanics and Dynamical Astronomy*, Vol. 135, Mar. 2023, doi: 10.1007/s10569-023-10129-4.

[13] M. A. Andreu, "Dynamics in the Center Manifold Around L2 in the Quasi-Bicircular Problem," *Celestial Mechanics and Dynamical Astronomy*, Vol. 84, No. 2, 2002, pp. 105–133, doi: 10.1023/a:1019979414586.

[14] D. B. Henry, J. Rosales, G. Brown, L. Peterson, D. Scheeres, and H. Smead, "Quasi-Periodic Orbits near Earth-Moon L1 in the Hill Restricted Four-Body Problem," *International Symposium on Space Technology and Science*, Kurume, Japan, July 2023.

[15] M. Jorba-Cuscó, A. Farrés, and Á. Jorba, "Two Periodic Models for the Earth-Moon System," *Frontiers in Applied Mathematics and Statistics*, Vol. 4, July 2018, doi: 10.3389/fams.2018.00032.

[16] D. J. Scheeres, "The Restricted Hill Four-Body Problem with Applications to the Earth-Moon-Sun System," *Celestial Mechanics and Dynamical Astronomy*, Vol. 70, No. 2, 1998, pp. 75–98, doi: 10.1023/a:1026498608950.

[17] G. W. Hill, "Researches in the Lunar Theory," *American Journal of Mathematics*, Vol. 1, No. 3, 1878, p. 245, doi: 10.2307/2369313.

[18] A. Wintner, *The Analytical Foundations of Celestial Mechanics*. Princeton: Princeton University Press, 1941.

[19] M. Hénon and J.-M. Petit, "Series expansions for encounter-type solutions of Hill's problem," *Celestial Mechanics*, Vol. 38, Jan. 1986, pp. 67–100, doi: 10.1007/bf01234287.

[20] M. Hénon, "Numerical Exploration of the Restricted Problem. V. Hill's case: Periodic orbits and their stability," *Astronomy and Astrophysics*, Vol. 1, 1969, pp. 223–238.

[21] G. W. Hill, "Researches in the Lunar Theory," *American Journal of Mathematics*, Vol. 1, No. 1, 1878, p. 5, doi: 10.2307/2369430.

[22] L. T. Peterson, G. Brown, Á. Jorba, and D. Scheeres, "Dynamics around the Earth–Moon triangular points in the Hill restricted 4-body problem," *Celestial Mechanics and Dynamical Astronomy*, Vol. 136, July 2024, doi: 10.1007/s10569-024-10203-5.

[23] D. B. Henry, J. J. Rosales, G. M. Brown, and D. J. Scheeres, "Quasi-periodic orbits around Earth-Moon L1 and L2 in the Hill restricted four-body problem," *AIAA/AAS Astrodynamics Specialist Conference*, Big Sky, Montana, American Institute of Aeronautics and Astronautics, Aug. 2023.

[24] Z. P. Olikara and D. J. Scheeres, "Numerical method for computing quasi-periodic orbits and their stability in the restricted three-body problem," *Advances in the Astronautical Sciences*, Vol. 145, Mar. 2012, pp. 911–930.

[25] R. R. Sanaga and K. Howell, "Analyzing the Challenging Region in the Earth-Moon L2 Halo Family via Hill Restricted Four-Body Problem Dynamics," *AIAA SCITECH 2024 Forum*, American Institute of Aeronautics and Astronautics, 2024.

[26] G. M. Brown, L. T. Peterson, D. B. Henry, and D. J. Scheeres, "Structure of Periodic Orbit Families in the Hill Restricted 4-Body Problem," *SIAM Journal on Applied Dynamical Systems*, 2024. In Review, doi: 10.48550/ARXIV.2402.19181.

[27] N. Baresi, *Spacecraft Formation Flight on Quasi-periodic Invariant Tori*. Phd thesis, University of Colorado Boulder, 2017.

[28] Z. P. Olikara, *Computation of Quasi-Periodic Tori and Heteroclinic Connections in Astrodynamics Using Collocation Techniques*. Phd thesis, University of Colorado Boulder, 2016.

[29] D. B. Henry, *Spacecraft Trajectory Design and Control Leveraging Quasi-periodic Orbits*. Phd thesis, University of Colorado Boulder, 2024.

[30] D. A. Lujan, *Methods to Explore Families of Quasi-Periodic Orbits with*. Phd thesis, University of Colorado Boulder, 2023.

[31] B. McCarthy, *Cislunar Trajectory Design Methodologies Incorporating Quasi-Periodic Structures with Applications*. Phd thesis, Purdue University, 2022.

[32] N. Baresi, Z. P. Olikara, and D. J. Scheeres, "Fully Numerical Methods for Continuing Families of Quasi-Periodic Invariant Tori in Astrodynamics," *The Journal of the Astronautical Sciences*, Vol. 65, Jan. 2018, pp. 157–182, doi: 10.1007/s40295-017-0124-6.

[33] G. Gómez and J. Mondelo, "The dynamics around the collinear equilibrium points of the RTBP," *Physica D: Nonlinear Phenomena*, Vol. 157, No. 4, 2001, pp. 283–321, doi: 10.1016/S0167-2789(01)00312-8.

[34] E. J. Doedel, V. A. Romanov, R. C. Paffenroth, H. B. Keller, D. J. Dichmann, J. Galán-Vioque, and A. Vanderbauwhede, "Elemental Periodic Orbits Associated with the Libration Points in the CircularRestricted 3-Body Problem," *International Journal of Bifurcation and Chaos*, Vol. 17, Aug. 2007, pp. 2625–2677, doi: 10.1142/s0218127407018671.

[35] Z. P. Olikara, G. Gómez, and J. J. Masdemont, *A Note on Dynamics About the Coherent Sun–Earth–Moon Collinear Libration Points*, pp. 183–192. Springer International Publishing, 2016.

[36] R. Seydel, *Practical Bifurcation and Stability Analysis*. Springer New York, 2010, doi: 10.1007/978-1-4419-1740-9.

[37] J. A. Dahlke and R. A. Bettinger, "Practical implementation of pseudo-arclength continuation to ensure consistent path direction," *Acta Astronautica*, Vol. 215, Feb. 2024, pp. 205–216, doi: 10.1016/j.actaastro.2023.12.007.

[38] Á. Jorba, "Numerical computation of the normal behaviour of invariant curves of n-dimensional maps," *Nonlinearity*, Vol. 14, July 2001, pp. 943–976, doi: 10.1088/0951-7715/14/5/303.